Forecasting and Diagnostic Analysis of Plume Transport around a Power Plant

J. A. Souto,* V. Pérez-Muñuzuri,+ M. deCastro,* M. J. Souto,+ J. J. Casares,* and T. Lucas#

Centro de Supercomputación de Galicia, Santiago de Compostela, Spain
+*Faculty of Physics, University of Santiago de Compostela, Santiago de Compostela, Spain*
#*Environmental Section, As Pontes Power Plant, As Pontes, Spain*

(Manuscript received 5 November 1996, in final form 11 December 1997)

ABSTRACT

A nonreactive Lagrangian atmospheric diffusion model is used for the simulation of SO_2 concentration around the As Pontes 1400-MW power plant located in northwestern Spain. This diffusion model has two kinds of input: 1) diagnostic wind fields from real measurements and 2) forecast wind fields from a 24-h mesoscale prediction.

This model-based system is applied for a particular day around the As Pontes 1400-MW power plant, which is a coal-fired power plant. The shape of estimated and forecast plumes are compared, and the meteorological prediction results are analyzed.

1. Introduction

The legal limits of pollution emission guarantee, for the majority of locations and under most meteorological situations, low ground-level concentrations. However, the existence of single sources of significant magnitude, or the danger of accidental emissions to the atmosphere, and also specific meteorological conditions may have an impact of the pollutant plume on the ground that may go beyond the direct legal air quality limits (for the pollutant ground-level concentration). To avoid the occurrence of these rare episodes, it is necessary to estimate the ground-level concentration that the emission legal limits would cause in the local environment in order to reduce the actual emission if the ground-level concentration goes up to the direct legal air quality limits. To obtain this estimation the combination of both a meteorological (diagnostic or prediction) model and an atmospheric diffusion model is used.

The As Pontes Power Plant is a 1400-MW coal-fired utility located in Galicia in northwestern Spain, which is an Atlantic region with very changeable weather and sea influence. Another important aspect is that diverse terrain and a great number of low hills and soft valleys can appear in short distances (less than 10 km), so turbulence complex terrain interactions can be significant.

When this power plant was installed, a 356.5 m above ground level (AGL) stack was erected to prevent any impact of the SO_2 plume at ground level. However, in some specific meteorological conditions, assumed air pollution or measured power plant emissions were set to modify operating conditions and even the quality of the coal to be burned.

The development of a system for air pollution estimation based on atmospheric modeling has already been suggested in the literature; for instance, Enger (1990) developed two combined models, meteorological and diffusion, for the simulation of plume transport at mesoscale distance.

In this paper, an air pollution control system for forecasting and real-time simulation and prediction of mesoscale plume transport, combined with an air pollution control network, is applied around the As Pontes 1400-MW power plant. The first version of this predictive system was described in Lucas et al. (1993). A description of the models included in this system, and some results of its application are shown here.

2. The model-based system

As the air pollution system aims at two different objectives, it can be divided in two subsystems. 1) Air pollution forecasting system: The result is a numerical meteorological prediction (wind, temperature, and turbulence) and a 3D distribution of SO_2 concentration for the following day. 2) Diagnostic system: From the last measured emission and meteorological data, the system performs a simulation of the plume transport; the result is 3D distributions of meteorological fields and SO_2 concentration for the current time.

The general scheme of the model-based system is shown in Fig. 1. For diagnostic purposes, the meteorological measurements available are the input to a di-

Corresponding author address: Dr. J. A. Souto, Centro de Supercomputacion de Galicia, Av. Vigo, s/n, 15706 Santiago de Compostela, Spain.
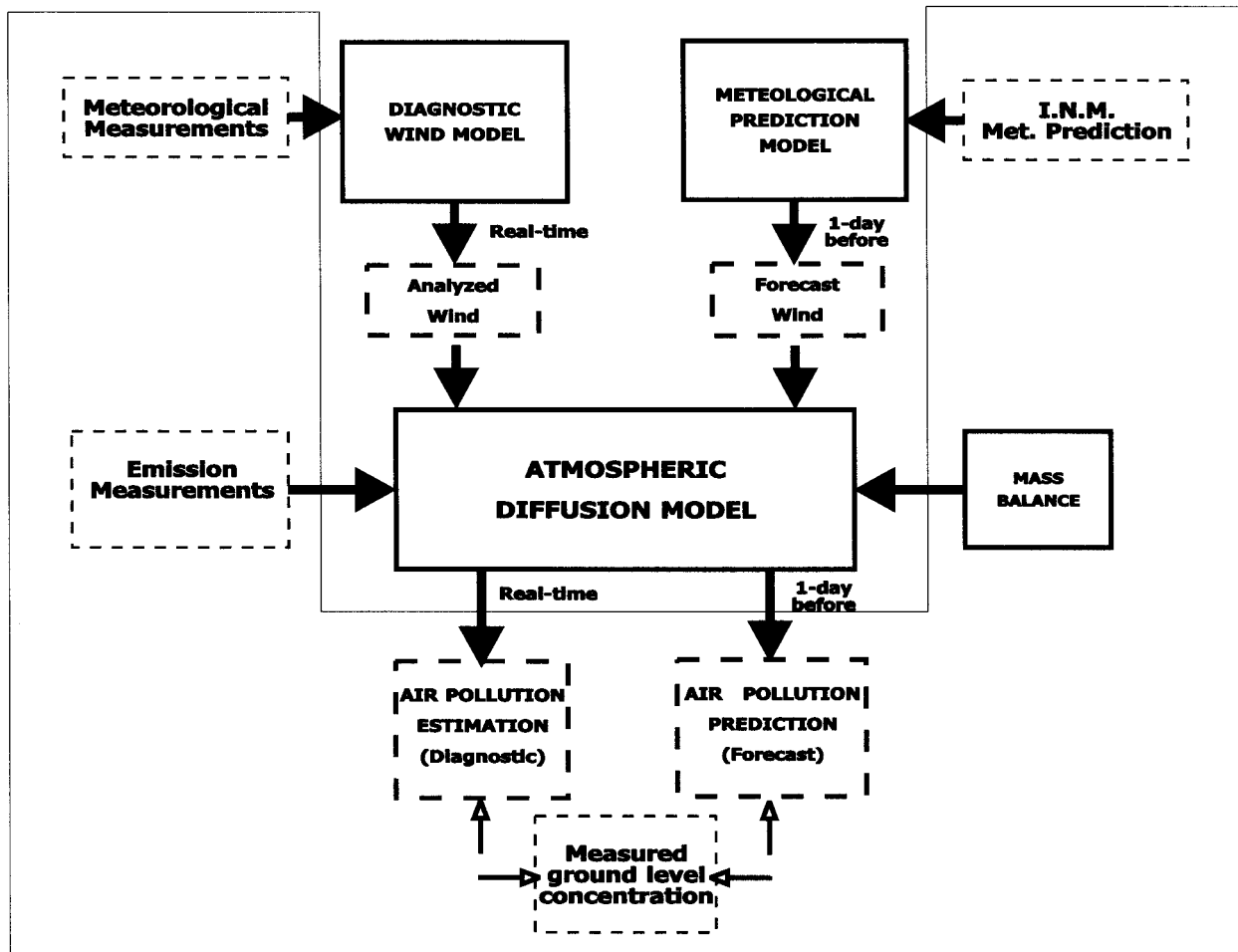E-mail: jas@cesga.es

FIG. 1. General scheme of the forecasting and real-time simulation plume transport system.

agnostic wind model (DWM) that estimates current 3D wind fields, temperature, and turbulence. With these estimations and the current emissions data, the atmospheric diffusion model (ADM) computes the SO_2 concentration distribution and the SO_2 ground-level concentration (glc) at the locations of the glc stations.

For the air pollution forecasting, the Spanish Meteorological Office provides a meso-α meteorological prediction in a coarse grid (around 100 km) with 6-h periods, which is applied by the meteorological prediction model (MPM) to define the initial and boundary conditions in a finer grid (2 km). The result is a 3D meteorological prediction of wind, temperature, and turbulence for the next day in 30-min averages.

An estimation of SO_2 emissions in the boilers is obtained as SO_2 concentration and flue gas flow, from the emissions mass balance (EMB), considering the composition and higher heating value of the coal; an average emission gas temperature of 190°C is assumed. With this emissions' estimation and the meteorological prediction, the ADM performs a 24-h simulation for the following day and obtains the predicted SO_2 concen-

tration distribution and SO_2 glc at the locations of the glc stations.

3. The diagnostic models

a. The diagnostic wind model (DWM)

For the calculation of meteorological fields in real time, an objective wind analysis (F. L. Ludwig, personal communication) was adopted. The wind fields estimation takes into account the influence of the terrain heights and the application of a nondivergence condition as the main physical constraint. To include these effects, DWM applies the critical streamline concept, based in the definition of airflow layers where the vertical motion is not physically allowed. An energy balance applied to an air mass (in a 3D wind field) initially located at a height z provides an expression of the height of the airflow layer that represents the flow of this air mass, in 2D, as follows:

$$H_c = z_g(1 - \text{Fr}), \qquad (1)$$

where z_g is the terrain height and Fr is the Froude number for the vertical motion as

$$\text{Fr} = \frac{\dfrac{u_c}{z}}{\left(\dfrac{g}{T}\dfrac{\partial \theta}{\partial z}\right)^{1/2}}, \tag{2}$$

where u_c is the horizontal wind velocity, g is the gravity acceleration, T is the absolute temperature, and $\partial \theta / \partial z$ is the lapse rate at the z height.

Equation (1) is applied at 20 layers to obtain the same number of airflow layers. After that, a null divergence condition is assumed for each airflow layer, and its slope is proportional to the vertical wind component, so the model develops 3D wind fields (as a set of 2D wind fields) in a short computing time.

In stable stratified conditions, the model can provide realistic 3D wind fields if good wind and temperature data are available, both at ground level and at different heights; but the vertical wind component calculated by the model is normally less than the actual wind in other meteorological situations. Then, vertical plume transport is mainly obtained from the plume growth.

The application of the critical streamline concept takes into account the influence of the atmospheric stability and the terrain heights in the vertical wind flow, and the null divergence condition corrects the horizontal wind flow due to the terrain; these effects cannot be represented by an interpolation of irregular horizontal wind measurements, especially the vertical wind flow.

b. The atmospheric diffusion model (ADM)

For the application of this system in an industrial plant, where a short time response is required, a Lagrangian puff model was chosen, such as the type of ADM that provides good single-plume transport estimations in a reasonable time. But, because of the significance of the variation of atmospheric conditions in height, a Lagrangian adaptive puff was adopted as the mathematical description of a plume volume (see Ludwig et al. 1989). The pollutant distribution into the puff is defined by means of a Gaussian function,

$$c = \frac{M}{\sqrt[3]{(2\pi)^2}\,\sigma_h^2 \sigma_z} \exp\left[-\frac{1}{2}\left(\frac{y}{\sigma_h}\right)^2\right] \exp\left[-\frac{\tilde{Z}^2}{2}\right], \tag{3}$$

where c is the pollutant concentration at the puff location defined by the transversal coordinate y and the nondimensional vertical coordinate $\tilde{Z}$, M is the mass pollutant in the puff, and σ_h and σ_z are the transversal and vertical standard deviations of the Gaussian concentration distribution. The nondimensional vertical coordinate $\tilde{Z}$ is defined as

$$\tilde{Z}(z) = \int_{Z_0}^{z} \frac{d\xi}{\sigma_z(\xi)}, \tag{4}$$

where Z_0 is the height of the lowest puff center and $\sigma(\xi)$ is the vertical standard Gaussian deviation at the ξ height. The model solves the Lagrangian approach in several steps as follows.

1) Generation of new adaptive puffs: Puffs are defined according to their volume, shape, and mass of pollutant; to calculate the minimum number of puffs that represent a continuous section of the plume, two factors are considered: wind speed, which affects the distance between the centers of different puffs, and horizontal turbulence, which affects the puff size in the wind direction. Typically, the model generates a new group of puffs every 60 s with the number of puffs varying due to the horizontal puff size.

2) Horizontal advection: The movement of the centers that define each puff location is calculated separately for the horizontal and vertical directions, depending on the horizontal wind components U, V at the puff location.

3) Horizontal diffusion: The horizontal puff size is defined by the standard deviation σ_h. In this application of the ADM to the As Pontes' environment, Draxler's expressions (Irwin 1983) were adopted as the most convenient.

4) Vertical advection and diffusion: In the adaptive puff, the vertical movement for each center defines both the vertical advection (because of the vertical wind component, W) and the vertical puff growth (because of the vertical diffusion, w_d). In addition, at the initial stages of the emission, the plume rise contribution (w_p) must be considered. So, the vertical movement for each center in a time step Δt is obtained as $z_{t+\Delta t} = z_t + (W + w_p + w_d)\Delta t$.

In the w_d calculation, again Draxler's expressions for vertical diffusion σ_z were applied. For the plume rise term, w_p, in unstable conditions, a range of values for the constants in Briggs's equation (Briggs 1972) proposed by Bennett et al. (1992) was tested. Finally, for unstable conditions the expression applied is

$$w_p = \frac{1.35 F^{1/3}}{\Delta t}\left[\frac{X^{0.58}}{v_h}\right], \tag{5}$$

where F is the buoyancy parameter, $v_h = (U^2 + V^2)^{1/2}$, and X is the travel distance.

For stable conditions, a different equation (Zhang and Ghoniem 1994) that includes the Brunt–Väisälä frequency, N, is adopted:

$$w_p = \frac{2.04}{\Delta t}\left\{\frac{0.86F[1 - \cos(NX/v_c)]}{N^2 v_c} + R_0^3\right\}^{1/3}, \tag{6}$$

where v_c is the wind speed at the stack top, R_0 is the stack radius, $N^2 = (g/\theta)(\partial \theta/\partial z)$, and θ is the potential temperature. Equation (6) is especially important at night. Although this plume rise is low, no nocturnal impacts are usually estimated because of

the short vertical plume growth in the nocturnal stable conditions.

5) Calculation of the SO_2 concentration: Finally, the pollutant concentration is calculated at the locations considered (usually, a regular 3D grid and the air pollution stations), adding the contribution of each puff to each location. Near ground, it is assumed that the pollutant is reflected to the air (that is, no deposition), so the estimated air pollutant concentration will be a maximum.

The coupled DWM–ADM system calculates current meteorological fields and plume transport for new emission and meteorological measurements every 5 min, so the power plant staff can follow the transport of the emitted plume in real time. The ADM is applied as a forecasting model too, when coupled to MPM and EMB, as described in section 4.

4. The forecasting models

a. Emissions mass balance (EMB)

The mass balance applied at the As Pontes Power Plant to estimate the coal consumption is adapted to calculate the SO_2 emission and flue gas conditions, using coal feeding, its composition, and the optimum air-to-coal rate.

b. Meteorological prediction model (MPM)

Plume transport is extremely sensitive to meteorological fields, so a high-resolution meteorological network is needed for real-time simulation. Plume transport forecasting also requires a highly precise meteorological prediction. With this goal, a meteorological prediction model has been developed for providing a good mesoscale meteorological prediction with small computing time cost.

For the MPM, it is feasible to combine two different points of view of analyzing meteorological data, namely, the standard atmospheric circulation models and a new approach based on the analysis of time series of observed data whose dynamics exhibit irregular or chaotic behavior. In the former case, physical information about weather and climate dynamics is obtained by studying the "bulk" properties (averages, covariances, etc.) of basic meteorological field variables. The latter case, which may be called "nonlinear time series analysis" (Farmer and Siderovich 1987; Casdagli 1989) explores the possibility and the extent to which the dynamics generating this time series is deterministic, that is, it occurs on a low-dimensional, chaotic attractor.

A full meteorological model should parameterize the subgrid-scale cloud dynamics in order to take into account its influence in the atmospheric flow and pollutants transport (Gimson 1997). To avoid these extensive calculations that require the use of high-performance computers, not available in an industrial plant, a method

for cloud cover dynamics (average cloud absorption) was developed based on nonlinear chaotic predictions (Pérez-Muñuzuri 1998). In this method, techniques of nonlinear analysis are applied to a time series of half-an-hour cloud-absorption values (averaged in space) obtained from infrared Meteosat images for 24-h forecasting. Later on, the obtained time series of average cloud absorption are inserted in a meteorological model for wind and temperature forecasting in the region of interest. This nonlinear method reveals the possibility of short-term prediction of atmospheric parameters whose dynamics would make it very difficult to obtain a prognostic equation by other means.

The present MPM is a 3D time-dependent mesoscale model based on finite difference solutions of the hydrothermodynamical equations. Only the hydrostatic part has been solved here (Souto et al. 1994, 1996; Pérez-Muñuzuri et al. 1996). A terrain-following coordinate system is used to introduce the topography in the model (Pielke and Martin 1981). The new vertical coordinate η is defined as

$$\eta = s\frac{z - z_g}{s - z_g},\tag{7}$$

where z_g is the terrain height. The maximum height s is taken constant in this study and equal to 7000 m. The basic equations of the model for the horizonatal wind components U and V, the potential temperature θ, and the specific humidity q_3 can be written as

$$\frac{dU}{dt} = \left\{\frac{s}{s - z_g}\right\}^2 \frac{\partial}{\partial \eta}\left(K_m \frac{\partial U}{\partial \eta}\right) - \theta\frac{\partial \pi}{\partial x}$$
$$+ g\left(\frac{\eta - s}{s}\right)\frac{\partial z_g}{\partial x} - \hat{f}W + fV,\tag{8a}$$

$$\frac{dV}{dt} = \left\{\frac{s}{s - z_g}\right\}^2 \frac{\partial}{\partial \eta}\left(K_m \frac{\partial V}{\partial \eta}\right) - \theta\frac{\partial \pi}{\partial y}$$
$$+ g\left(\frac{\eta - s}{s}\right)\frac{\partial z_g}{\partial y} - fU,\tag{8b}$$

$$\frac{d\theta}{dt} = \left\{\frac{s}{s - z_g}\right\}^2 \frac{\partial}{\partial \eta}K_h \frac{\partial \theta}{\partial \eta} + S_\theta,\tag{8c}$$

and

$$\frac{dq_3}{dt} = \left\{\frac{s}{s - z_g}\right\}^2 \frac{\partial}{\partial \eta}K_q \frac{\partial q_3}{\partial \eta},\tag{8d}$$

where f and $\hat{f}$ denote the Coriolis parameters ($f = 1.45 \times 10^{-4} \sin(\phi)s^{-1}$, $\hat{f} = 1.45 \times 10^{-4} \cos(\phi)s^{-1}$, and ϕ is the latitude at the area under consideration that, in general, will be a function of the position $[x, \phi(x)]$. Finally, to complete the calculations of the wind field, the vertical component of the wind velocity, W, is obtained from the conservation of mass relationship.

The vertical turbulent fluxes, K_m, K_h, and K_q, in Eqs.

TABLE 1. Values for the soil properties α_s, ρ_s, c_s, k_s, and z_0 used in the MPM model.

	α_s	z_0 (m)	$\rho_s \times 10^{-3}$ (kg m^{-3})	c_s (J kg^{-1} K^{-1})	$k_s \times 10^6$ (m^2 s^{-1})
Urban area	0.18	0.50	2.3	879	2.30
Agriculture	0.20	0.15	0.4	2302	0.12
Forest	0.10	0.80	0.3	1256	0.30
Wetland	0.14	0.10	1.1	3650	0.12
Water	*	10^{-4}	1.0	4186	0.15

* For water surface an expression for the albedo as a function of the solar zenith angle Z was used: $\alpha_s = -0.0139 + 0.0467 \tan Z$; $0.03 \le \alpha_s \le 1$.

TABLE 2. Typical values of cloud absorption ξ.

Cloud type	ξ
High cloud	0.20
Middle cloud	0.56
Low cloud other than cumulonimbus	0.59
Cumulonimbus	0.95

(8a)–(8d) account for the vertical mixing in the atmosphere, and their definition depends on the stability of the layer being simulated. When the layer is stably stratified, a parameterization based on the Richardson number suggested by Blackadar (1979) is used. On the other hand, when the atmospheric layer is unstably or neutrally stratified, the exchange coefficients are then defined as a function of the distance above the ground and the O'Brien's (1970) cubic polynomial approximation is used. To apply this profile formulation, the depth of the planetary boundary layer (PBL) must be known.

The depth of the PBL, z_i, is usually associated with an inversion, and it is calculated, during the daytime, as suggested by Deardorff (1974) and Pielke and Mahrer (1975), by a prognostic equation mainly depending on the surface heating (Pielke 1984). With the use of this slab model, which considers the entrainment layer infinitesimal, Deardorff has derived the following equation for the growth of the convective PBL, which includes the effects of the entrainment:

$$\frac{\partial z_i}{\partial t} = -u_{z_i}\frac{\partial z_i}{\partial x} - v_{z_i}\frac{\partial z_i}{\partial y} + w_{z_i} + \frac{1.8(w_*^3 + 11u_*^3 - 33u_*^2 f z_i)}{g\frac{z_i^2}{\theta_s}\gamma + 9w_*^2 + 7.2u_*^2}, \quad (9)$$

where w_* is estimated from a formulation based on the turbulent parameters u_* and θ_*, θ_s is the potential temperature at the surface layer, and γ is the potential temperature lapse rate at z_i (Pielke 1984).

During the transition from convective to stable conditions Eq. (9) cannot be applied since the observed z_i tends to adjust exponentially toward an equilibrium depth (Kondratyev 1969). The expression of Smeda (1979), who proposed that the growth of the stable layer is proportional to the stress induced by the wind near the surface, is used:

$$z_i^{\text{eq}} = 0.3u_*/f. \quad (10)$$

The height calculated by Eq. (10) during transition time could be considered as a fictitious height during which the stable layer near the surface develops and becomes

well established, so the model provides a value for the PBL during all the periods of the simulation.

The similarity stability functions given by Businger are used to account for the turbulence parameters needed to solve Eqs. (9) and (10). The values for q_*, θ_*, and u_* are obtained by applying the two-level method proposed by Berkowicz and Prahm (1982). This method starts evaluating the friction velocity and the potential temperature scale through the differences between the wind speed and temperature at the two lowest levels of the model grid—$z_1 = 1$ m and $z_2 = 3$ m:

$$u_* = \frac{k\Delta u}{\ln z_2/z_1} \quad \text{and} \quad \theta_* = \frac{k\Delta\theta}{0.74 \ln z_2/z_1}. \quad (11)$$

Then the initial Monin–Obukhov length, L, is obtained by $L = u_*^2\overline{\theta}/kg\theta_*$.

With this initial value, the integrated forms of the Businger functions (ϕ_m and ϕ_h) (Businger et al. 1971) can be calculated and used to obtain new u_* and θ_* values by

$$u_* = \frac{k\Delta u}{[\ln z_2/z_1 - \phi_m(z_2/L) + \phi_m(z_1/L)]} \quad (12)$$

and

$$\theta_* = \frac{k\Delta\theta}{0.74[\ln z_2/z_1 - \phi_h(z_2/L) + \phi_h(z_1/L)]}. \quad (13)$$

The new Monin–Obukhov length would be

$$L = \left[\frac{\overline{\theta}(\Delta u)^2}{g\Delta\theta}\right] 0.74 \frac{\ln z_2/z_1 - \phi_h(z_2/L) + \phi_h(z_1/L)}{[\ln z_2/z_1 - \phi_m(z_2/L) + \phi_m(z_1/L)]^2}. \quad (14)$$

The process is repeated iteratively until it verifies $|L_f - L_{f-1}| \le 0.1|L_f|$.

1) NUMERICAL RESOLUTION

Equations (8a)–(8d) are solved by a finite difference method. A forward-in-time, upstream-in-space scheme is used for the advection terms. For the diffusion terms (vertical turbulent fluxes), a semi-implicit scheme with a weight of 75% on a future time step is used and a constant time step of 30 s. The rest of spatial derivatives are solved by a forward-in-time, centered-in-space scheme. For Coriolis terms, as well as for the radiation terms, an explicit scheme has been used.

By using an upwind scheme for the advection terms, nonlinear waves appear, disturbing the solution, then,
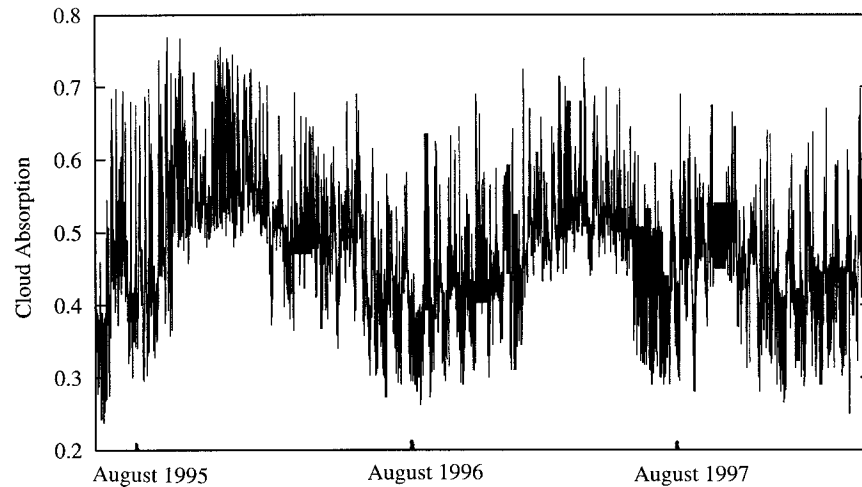
FIG. 2. Cloud absorption ξ time series of half-hour measurements in northwestern Galicia, Spain, obtained from the Meteosat IR images and consisting of 40 000 data observations. Values range from 0 (no absorption of solar radiation) to 1 (total absorption).

although an eddy parameterization of the horizontal turbulent fluxes has been selected to minimize these effects, a 2D filtering based on the averaging of *U, V, W, θ,* and q_3 with the nearest neighbors with some factor α (Haltiner and Williams 1980) has also been applied.

At the finite difference grid, 40 vertical levels beginning at 1 m above the ground spaced logarithmically until reaching the top at $s = 7000$ m and 31×31 grid points on each vertical level with a grid mesh of 2000 m have been used.

Both the continuity equation and the hydrostatic pressure relation are integrated by an explicit finite-difference scheme in order to obtain the vertical component *W* of the wind velocity and the scaled pressure. To avoid the first spurious effects due to initialization, the model is run during 1 h with the requirement that no time-dependent forcing terms are permitted to occur.

2) BOUNDARY CONDITIONS

Lateral boundary conditions at each level are constant inflow and zero gradient outflow for the horizontal wind components and zero-flux boundary conditions for pressure, potential temperature, and specific humidity. Besides, surface temperature and specific humidity are initialized from measurements obtained from nine meteorological towers in the area under study. An initial constant profile for q_3 is supposed until reaching the PBL and from there on, q_3 linearly decreases to zero. The depth of the PBL, z_i, initially, at night, is assumed to be very small and here was set to 100 m.

In the terrain-following coordinate system, z_g is defined as the sum of the terrain height, the zero displacement, and the surface roughness length. Then, by definition, the wind at $\eta = 0$ is equal to zero. The derivatives of the horizontal wind components at the upper

boundary are set to zero (i.e., homogeneous geostrophic wind). The vertical gradient of temperature and humidity at the model top are assumed constant. The temperature at the ground is calculated by means of a force–restore method, while humidity at the ground surface is calculated by a method proposed by McCumber and Pielke (1991) that mainly depends on the surface temperature.

The following Eq. (15), termed the "force–restore method" by Deardorff (1978), was used to predict the air–earth interface temperature T_G,

$$\frac{\partial T_G}{\partial t} = \frac{1}{\rho_s c_s}\left(\frac{4\pi}{k_s \tau}\right)^{1/2}[(1 - \alpha_s)Q_S + Q_{LD} - Q_{LU} - Q_H - Q_E]$$

$$- \frac{2\pi(T_G - T_M)}{\tau}, \qquad (15)$$

where

α_s	albedo of surface,
Q_S	solar radiative flux,
Q_{LD}	downward longwave radiation,
Q_{LU}	upward longwave radiation,
Q_H	sensible heat flux from earth to atmosphere,
Q_E	latent heat flux,
ρ_s	density of soil,
c_s	heat capacity of soil per unit mass,
k_s	thermal diffusivity of soil,
τ	24 h, and
T_M	deep soil temperature.

The last term in Eq. (15) includes the effect of conduction from the ground below the interface. It avoids the problem of having to compute temperatures at a number of levels beneath the surface. The variable T_M is set equal to the daily mean temperature for the time of simulation.

TABLE 3. Location of the As Pontes Power Plant and the meteorological towers, ground-level concentration monitoring remote stations, and sodar equipment located around it. The letters (A–H) in the monitoring stations' nomenclature corresponds to the approximate pollutants' plume direction that affects the station, so usually most of the monitoring stations with the same letter are affected along the same air pollution episode.

Air pollution monitoring station	Influenced sector	Longitude (UTM, km)	Latitude (UTM, km)	Meteorological tower?
A-6	A (0°–45°)	583.8	4837.0	Yes
B-1	B (45°–90°)	593.3	4811.7	No
B-2	B (45°–90°)	602.1	4820.7	No
B-6	B (45°–90°)	609.2	4816.0	Yes
B-7	B (45°–90°)	616.2	4827.9	Yes
C-8	C (90°–135°)	602.2	4807.4	No
C-9	C (90°–135°)	606.0	4796.3	No
D-6	D (135°–180°)	591.1	4790.1	No
E-3	E (180°–225°)	581.2	4798.3	Yes
F-2	F (225°–270°)	582.0	4806.2	Yes
F-4	F (225°–270°)	573.2	4805.6	No
F-5	F (225°–270°)	566.4	4798.7	Yes
F-6	F (225°–270°)	577.6	4805.9	No
F-7	F (225°–270°)	575.3	4809.9	Yes
G-2	G (270°–315°)	578.3	4822.8	No
G-4	G (270°–315°)	576.5	4815.3	Yes
H-1	H (315°–360°)	586.5	4817.7	No
Power plant	—	593.0	4810.3	No
Sodar	—	592.6	4809.0	Yes

The soil properties α_s, ρ_s, c_s, k_s, and, additionally, z_0 (surface roughness) depend on the surface nature. The values used are included in Table 1. The values of the heat flux Q_S, Q_{LD}, Q_{LU}, Q_H, and Q_E may change with time and they have been calculated following parameterizations described in Pielke (1984) and Stull (1991). The solar radiative flux, Q_S, is computed from the following expression:

$$Q_S = [1 - \xi(t)](S - A_S) \cos Z, \qquad (16)$$

where S is the effective solar constant, A_S is the absorption by atmospheric gases, Z is the solar zenith angle, and ξ is the sum of the cloud-top albedo and in-cloud absorption by cloud droplets, as an equivalent albedo. The value of ξ can change with time. Clouds are assumed to consist of one layer at a height, which is the average height, weighted by the amount of each layer observed from the surface. Typical values of ξ are shown in Table 2.

The downward and upward longwave radiation flux (Prata 1996) are calculated by one formulation given by Idso and Jackson (1969),

$$Q_{LD} - Q_{LU} = \sigma\{[E_a(1 - \xi(t)) + \xi(t)]T_a^4 - T_G^4\}, \qquad (17)$$

where

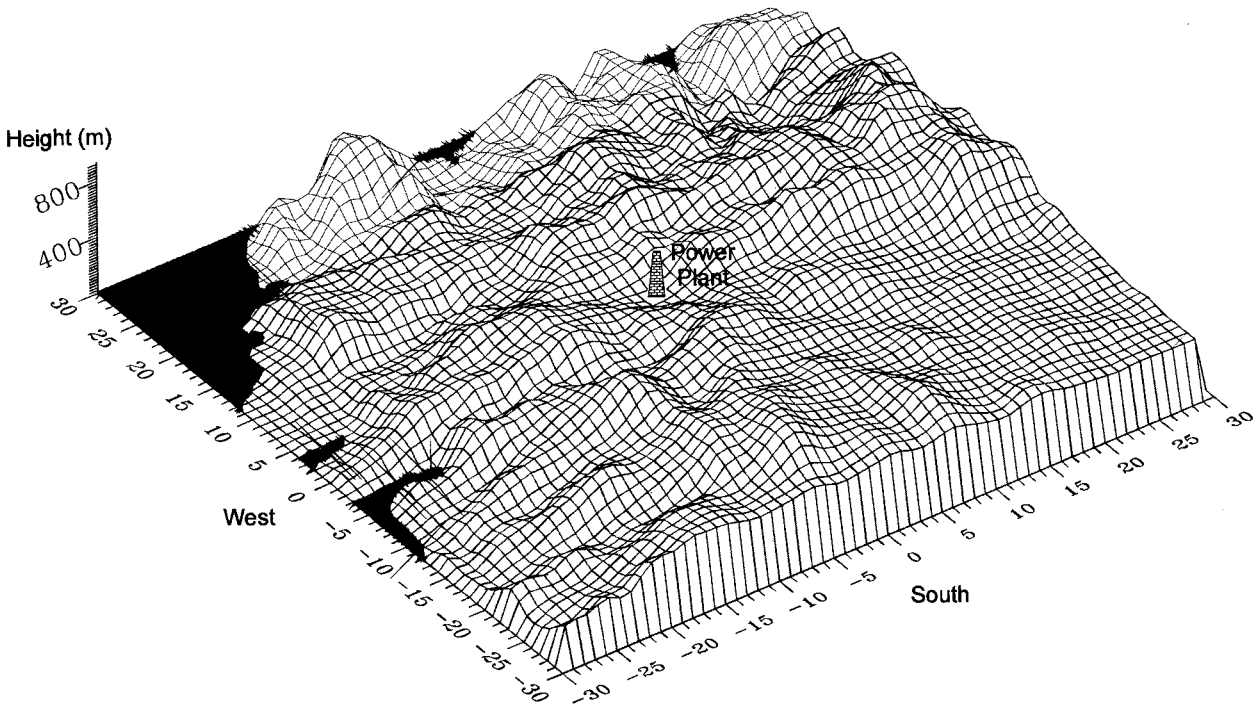$$E_a = 1 - 0.261 \exp[-7.77 \times 10^{-4}(273 - T_a)^2], \qquad (18)$$

FIG. 3. A 3D representation of the topography of the area under study, 30 km around the As Pontes Power Plant. Horizontal grid scales are in kilometers.
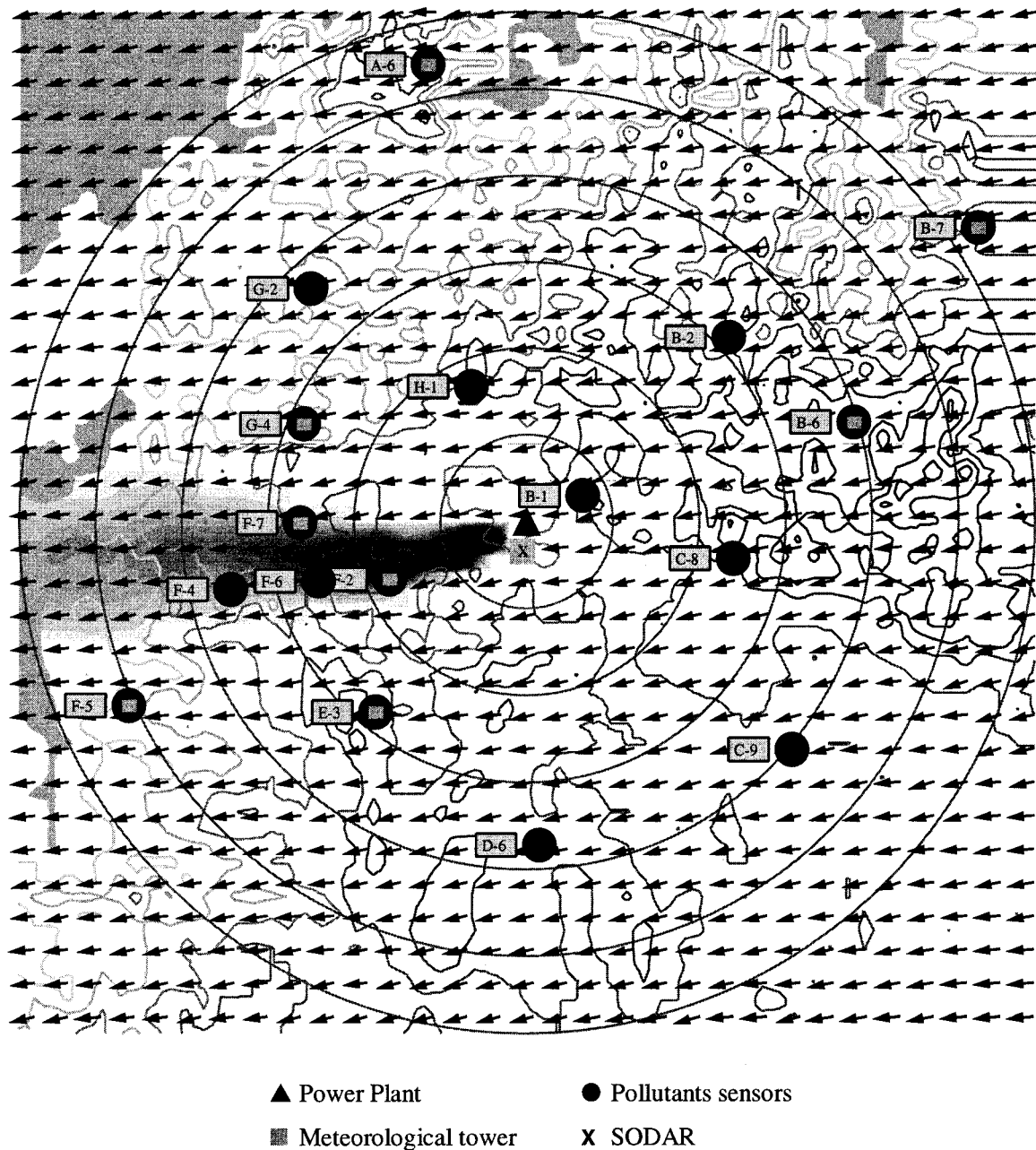
FIG. 4. Horizontal plume dispersion and wind field estimated by the diagnostic system. Wind vector plots represent constant-height surfaces for the main plume transport level (500 m AGL) at 1700 LST 5 March 1996. The contour lines represent the terrain altitude in 100-m intervals. Note this map shows the location of the power plant, the nine meteorological towers, the sodar equipment, and the 17 SO$_2$ ground-level concentration remote stations.

and T_a is determined at Stevensen screen height (1.5 m). Finally, Q_H and Q_E are calculated as

$$Q_H + Q_E = -\overline{\rho}u_*(C_p\vartheta_* + L_vq_*). \quad (19)$$

On the other hand, for the air–water interface, a formulation given by Blanke and Delecluse (1993), has been used. Here, as well, heat fluxes depend on the cloud absorption parameter.

3) ESTIMATION OF THE EQUIVALENT ALBEDO

Equations (8)–(19) are used to forecast the meteorological conditions 24 h in advance and a continuous set of values of ξ must be provided in order to close the model. With this objective, we have collected a time series of values of equivalent albedo, ξ, during one year and a half-year from semihourly infrared im-
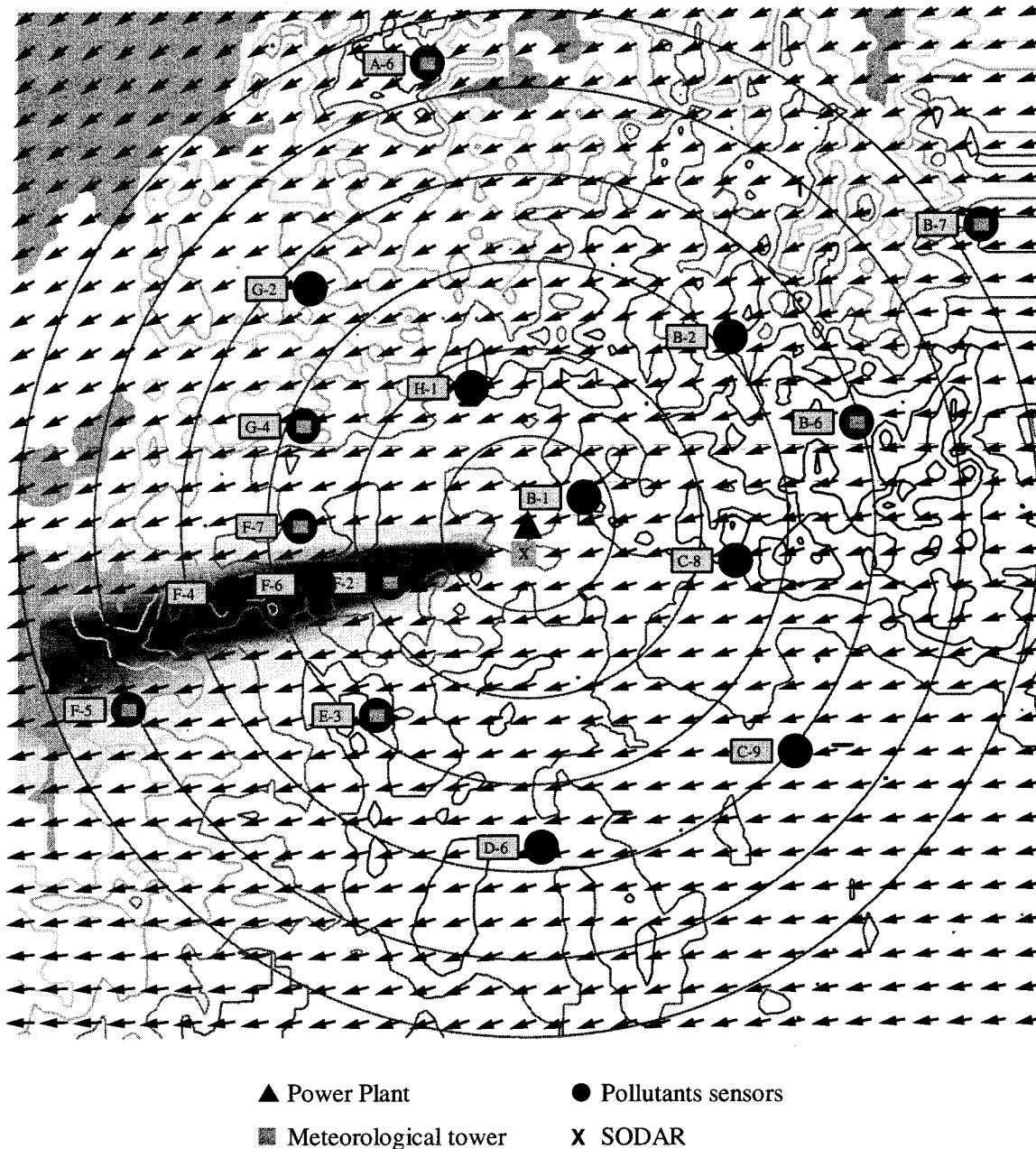
FIG. 5. Horizontal plume dispersion and wind field calculated by the prediction system one day before. Wind vector plots represent constant-height surfaces for the main plume transport level (500 m AGL) at 1700 LST 5 March 1996.

ages of western Europe provided by the Meteosat at the region of interest in order to predict its behavior (Fig. 2). From these images, an average-in-space value of the cloud covering of the area of interest (northwestern Spain) is sampled as a single dataset ranging from 0 to 1 ($\xi = 1$ means that no radiation emitted from the earth's surface is detected by the Meteosat). For a clear sky, the stored value is close to zero, while intermediate values depend on cloud thickness and water phase and content. On the other hand, $\xi(t)$ could be considered to depend on x and y as well—$\xi(x, y,$

t). But by doing so, it will require a higher precision in the satellite images that is not the case with the Meteosat. In the actual system, the amount of noise in the time series increases with the discretization of the image, which deteriorates the precision of the nonlinear forecasting method used here (Pérez-Muñuzuri 1998).

Note in Fig. 2 that the series looks irregular, although clearly two periodicities can be stated: 1) the annual frequency (it is usually more cloudy in winter than in summer) and 2) the daily frequency (during the day the amount of radiation reflected by the earth is greater than

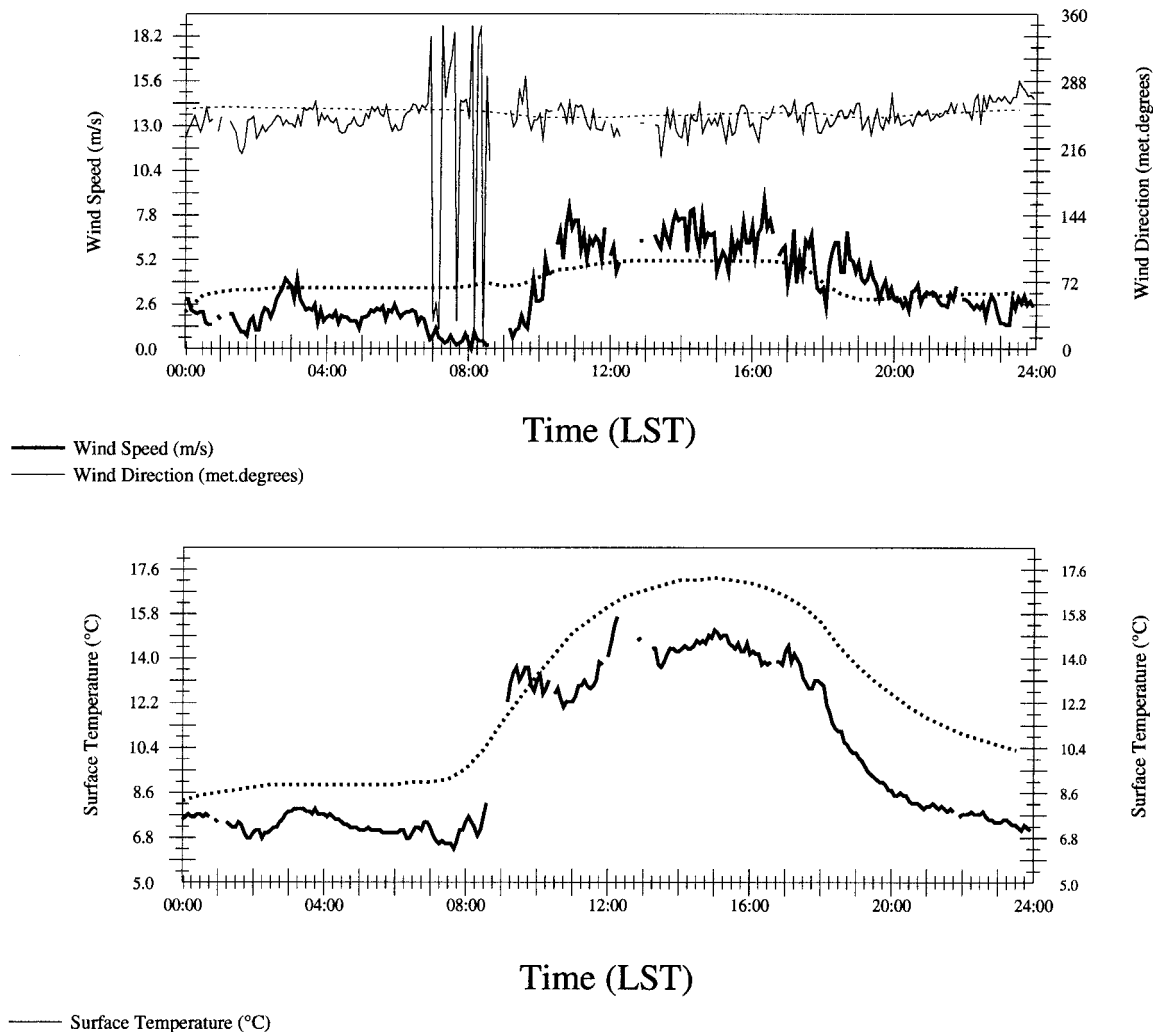# F-5 Meteorological & Pollutants Station

Date : 05/March/1996

FIG. 6. Predicted (dotted line) vs observed (solid line) wind (velocity and direction) and temperature at the F-5 station, 25 km southwest from the power plant, where the plume is near ground level, 5 March 1996.

during the night). In other words, the time evolution of cloud cover and its irregular behavior should be taken into account for a good description of the heat fluxes given by the set of Eqs. (16)–(19).

5. Results

For diagnostic plume transport, continuous emissions monitoring and wind (10 m AGL) and temperature (2 m AGL) measurements from nine meteorological towers arrive to the system every 5 min; in addition, wind and turbulence measurements from a Remtech PA-3 sodar

are obtained every 30 min (Table 3). These data are connected to the models, as shown in Fig. 1.

As an example of the models' application, results of both diagnostic and forecasting of the plume on 5 March 1996 are included. At this date, middle clouds and strong easterly winds occurred as the main meteorological patterns.

Figure 3 shows a 3D representation of the topography of the environment considered. Figures 4 and 5 show the predicted horizontal plume dispersion from the stack at 1700 LST, as obtained by the diagnostic and prediction models, respectively. Wind vector plots are repre-
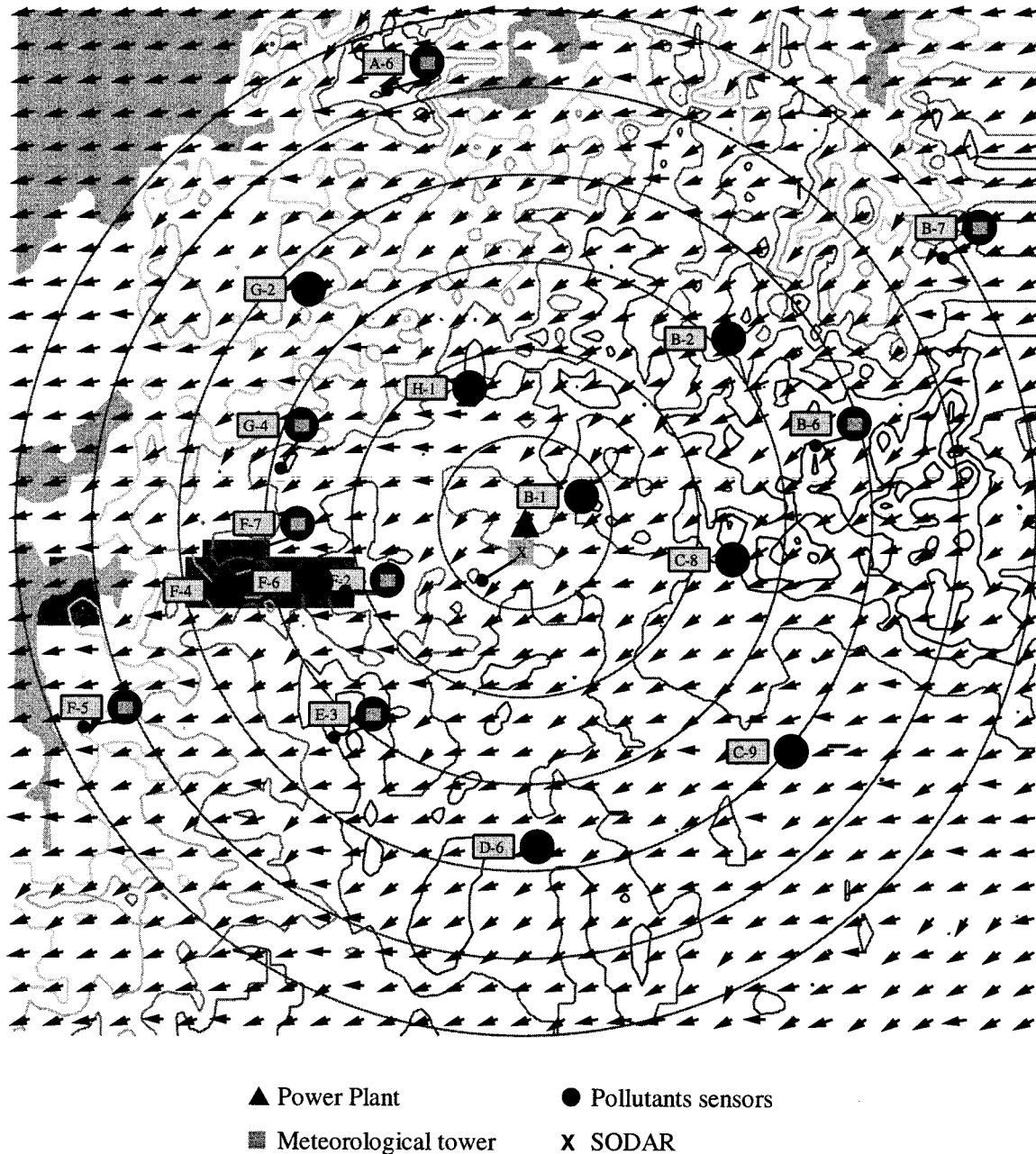
FIG. 7. Plume impact estimated by the diagnostic system. Wind vector plots represent constant-height surfaces for the lowest model level (10 m AGL). The symbol represents observed wind directions at the nine meteorological stations at 1700 LST 5 March 1996.

sented for the main transport level of the plume. A symbol at each meteorological station represents the observed wind direction that is plotted for comparison. Note that predicted wind fields show a better agreement with the experimental observed winds than those calculated with the diagnostic model because of the diagnostic wind direction in height depends mainly on the wind direction provided by one sodar, so any deviation of the sodar measurements determine a deviation of the wind flow in height. On the other hand, the horizontal

plume growth rate is similar in both figures, although there is a small deviation of the plume centerline near the boundary between both results. The time evolution of the wind speed and direction predicted at the F-5 station shown in Fig. 6 shows a reasonable agreement with the measured time series.

The SO_2 ground-level concentrations estimated by the diagnostic and prediction models are shown in Figs. 7 and 8, respectively. For comparison, the image shown in Fig. 9 represents the interpolated SO_2 ground-level
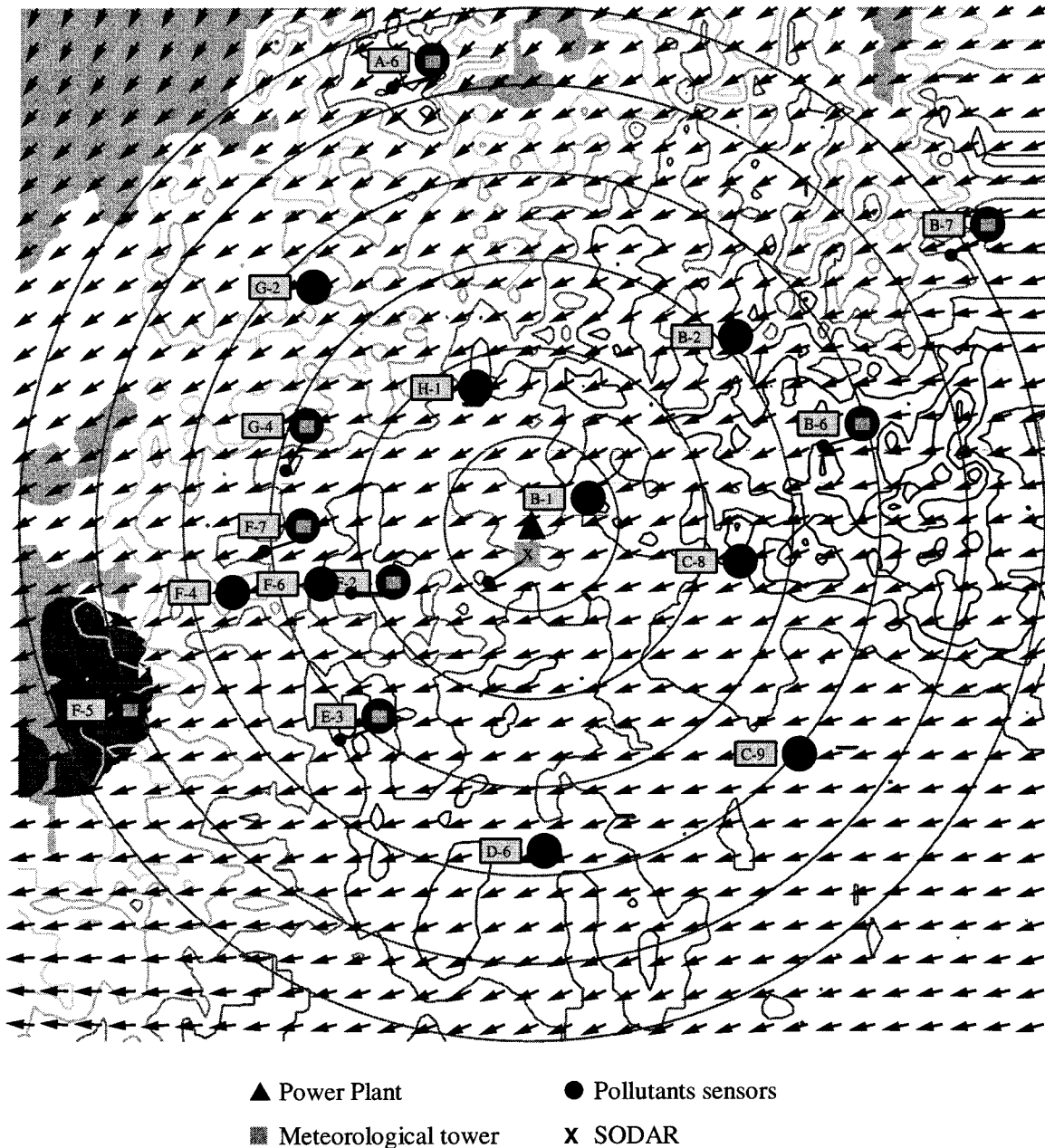
FIG. 8. Plume impact calculated by the prediction system. Wind vector plots represent constant-height surfaces for the lowest model level (10 m AGL). The symbol represents observed wind directions at the nine meteorological stations on 1700 LST 5 March 1996.

concentration measurements observed at the glc stations. Low SO_2 glc (less than 100 μg m^{-3}) were detected on stations F-2, F-4, and F-5, so no significant plume impact was observed. But, the observed SO_2 glc in Fig. 9 shows that the main plume impact appears between F-2 and F-4 stations, as in the diagnostic impact (Fig. 7); on the other hand, predicted impact is estimated around the F-5 station. About the plume trajectory, predicted plume follows the actual plume trajectory better than the diagnostic plume, due to the fact that the simulated trajectory depends mainly on the sodar data, and

a slightly different wind measurement in height provided by the sodar can produce these deviations. On the other hand, the diagnostic wind direction at surface level (Fig. 7) is very similar to surface measurements, as DWM reproduces the effect of the local topography over the wind flow; the predicted surface wind direction (Fig. 8) is more homogeneous.

Figures 10 and 11 show the vertical plume growth of diagnostic and predicted plumes, at 1700 LST. The diagnostic plume growth is higher, so the simulation estimates a plume impact nearer the source (between F-
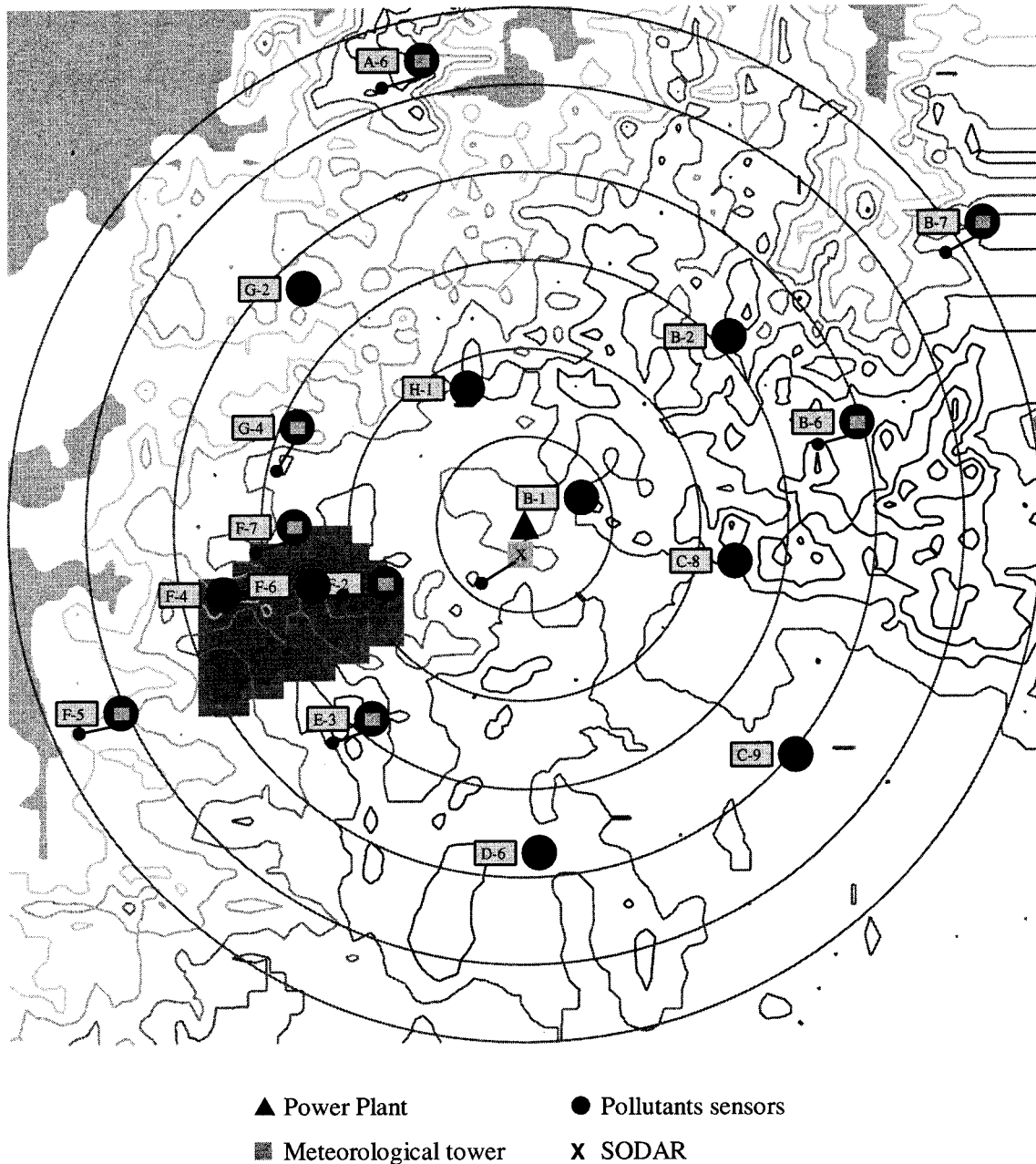
FIG. 9. Plume impact interpolated from SO_2 ground-level concentration measurements observed at the 17 glc stations system. The symbol represents observed wind directions at the nine meteorological stations on 1700 LST 5 March 1996.

2 and F-4) than the predicted (over F-5), as it was shown in Figs. 8 and 9, respectively. Here, the observed diagnostic wind profiles are more homogeneous than those described by the predicted model. In other words, the vertical motion of the wind flow, which is responsible for the motion of the plume and ultimately for glc impacts, is stronger in the prediction model, so the predicted plume impact goes farther than the observed.

In Fig. 12, predicted and measured σ_w values are compared. Both of them fit well until the inversion layer,

600 m above the terrain; above this height, a constant value of 0.03 m s^{-1} for σ_w is assumed. Note that the measured σ_w is slightly different than the predicted one, as this fact is in agreement with the different vertical plume growth described above.

6. Conclusions

Diagnostic and daily forecasting of plume transport around a power plant is performed by a model-based
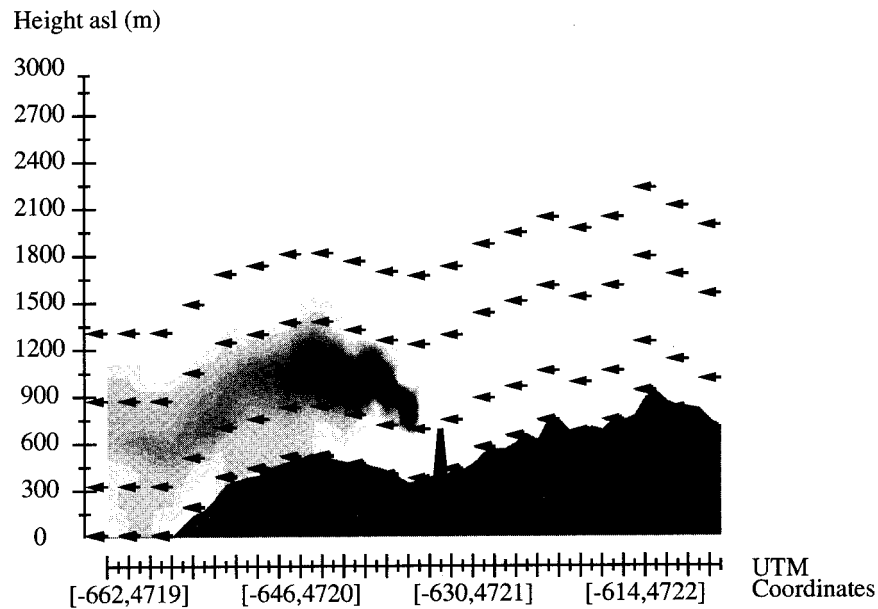
Height asl (m)

Fig. 10. Vertical plume growth of the diagnostic plume and wind profile estimated by the diagnostic system at 1700 LST 5 March 1996. Topography below the plume centerline is shown with the altitude in meters (ASL).

system. A plume transport diagnostic can run on a work-station and a new meteorological condition is considered every 5 min, coupling a DWM and an ADM that uses Lagrangian adaptive puffs. Forecasting of plume transport combines a meso-β MPM to the ADM too.

The plume transport forecast is being used as a decision support tool by the power plant staff, especially to know 24 h in advance the risk of plume impact on

the surroundings. In addition, the plume transport diagnostic helps them to follow the possible impact of the actual emissions.

Results of the simulation of the plume transport, using the diagnostic and prediction system, for 5 March 1996 are compared to the observed plume impact. As the major result, both diagnostic and predicted plumes impact the ground level at the same hour as the observed
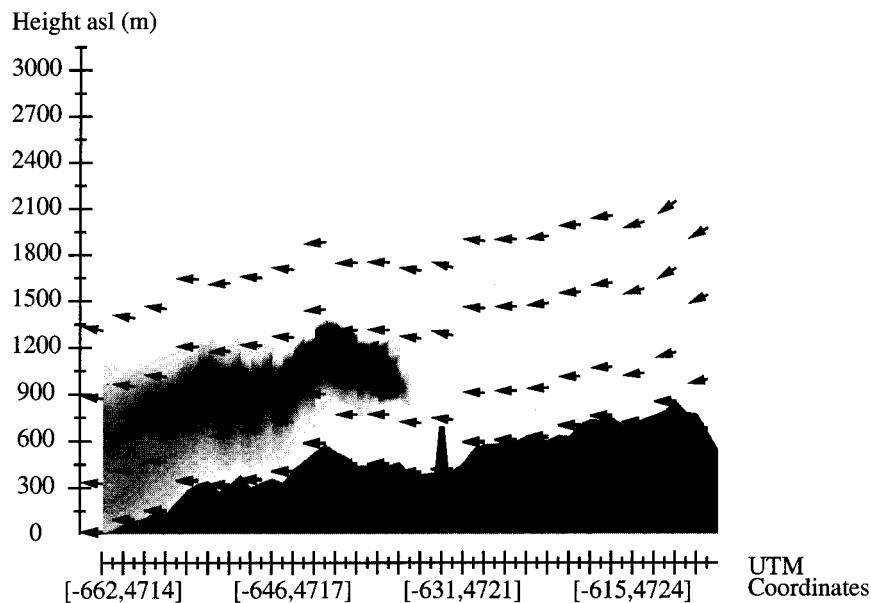
Height asl (m)

Fig. 11. Vertical plume growth of the predicted plume and wind profile calculated by prediction system at 1700 LST 5 March 1996. Topography below the plume centerline is shown with the altitude in meters (ASL).
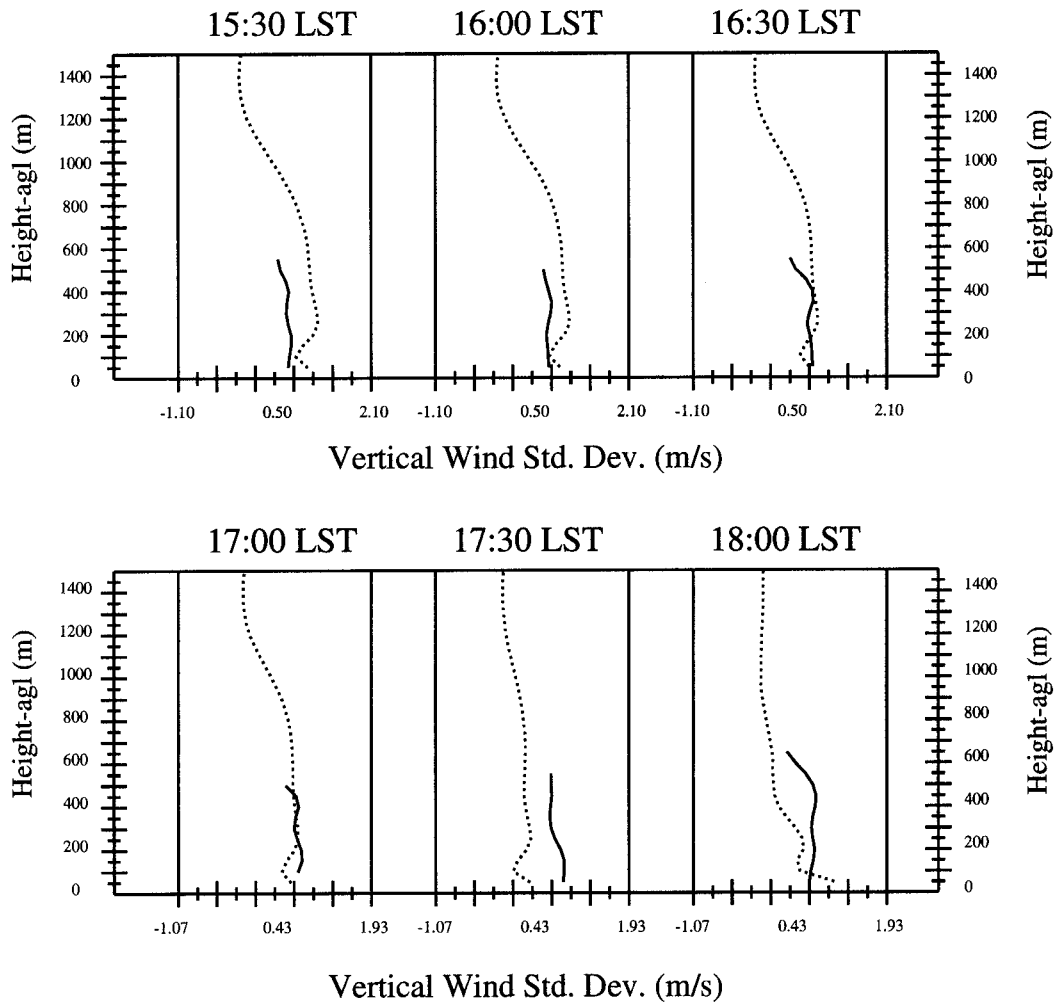
SODAR
Date : 05/March/1996

FIG. 12. Measured (solid line) and predicted (dotted line) vertical wind standard deviation, σ_w, from 1600–1800 LST 5 March 1996.

impact; in addition, the diagnostic plume impact agrees with the observed impact better than the predicted one. The deviations of the diagnostic plume direction are mainly due to the fault in the wind measurements provided by the sodar.

Although the qualitative behavior of the plume is well described by the model-based system, as it was shown for the simulations on 5 March 1996, the quantitative results of the simulations indicate that several uncertainties are unsolved. Specifically, new solutions for the prediction of the atmospheric stability, which characterizes the plume rise and plume growth, will be tested in the future; and the use of a Lagrangian particle model is planned only for forecasting because its computing time cost is an important drawback to diagnostic application.

REFERENCES

Bennett, M., S. Sutton, and D. R. C. Gardiner, 1992: An analysis of LIDAR measurements of buoyant plume rise and dispersion at five power stations. *Atmos. Environ.,* **26A,** 3249–3263.

Berkowicz, R., and L. P. Prahm, 1982: Evaluation of the profile method for estimation of surface fluxes of momentum and heat. *Atmos. Environ.,* **16,** 2809–2819.

Blackadar, A. K., 1979: High-resolution models of the planetary boundary layer. *Adv. Environ. Sci. Eng.,* **1,** 50–85.

Blanke, B., and P. Delecluse, 1993: Variability of the tropical Atlantic

Ocean simulated by a general circulation model with two different mixed-layer physics. *J. Phys. Oceanogr.,* **23,** 1363–1388.

Briggs, G. A., 1972: Discussion of chimney plumes in neutral and stable surrounding. *Atmos. Environ.,* **6,** 507–510.

Businger, J. A., J. C. Wyngaard, T. Izumi, and E. F. Bradley, 1971: Flux-profile relationships in the atmospheric surface layer. *J. Atmos. Sci.,* **28,** 181–189.

Casdagli, M., 1989: Nonlinear prediction of chaotic time series. *Physica D,* **35,** 335–356.

Deardorff, J. W., 1974: Three-dimensional numerical study of the height and mean structure of a heated planetary boundary layer. *Bound.-Layer Meteor.,* **7,** 81–106.

——, 1978: Efficient prediction of ground surface temperature and moisture, with inclusion of a layer of vegetation. *J. Geophys. Res.,* **83,** 1889–1903.

Enger, L., 1990: Simulation of dispersion in moderately complex terrain. Part A: The fluid dynamic model. *Atmos. Environ.,* **24A,** 2431–2446.

Farmer, J. D., and G. G. Siderowich, 1987: Predicting chaotic time series. *Phys. Rev. Lett.,* **59,** 845–848.

Gimson, N. R., 1997: Pollution transport by convective clouds in a mesoscale model. *Quart. J. Roy. Meteor. Soc.,* **123,** 1805–1828.

Haltiner, G. J., and R. T. Williams, 1980: *Numerical Prediction and Dynamic Meteorology.* John Wiley and Sons, 450 pp.

Idso, S. B., and R. D. Jackson, 1969: Thermal radiation from the atmosphere. *J. Geophys. Res.,* **74,** 3397–3403.

Irwin, J. S., 1983: Estimating plume dispersion—A comparison of several sigma schemes. *J. Climate Appl. Meteor.,* **22,** 92–114.

Kondratyev, J., 1969: *Radiation in the Atmosphere.* Academic Press, 212 pp.

Lucas, T., J. Abadía, J. J. Casares, and J. A. Souto, 1993: Development of an emissions control system for a coal-fired power plant. *Proc. Second Int. Conf. on Combustion Technologies for a Clean Environment,* Lisbon, Portugal, Gulbekian Foundation, 9–16.

Ludwig, F. L., R. Salvador, and R. Bornstein, 1989: An adaptive volume plume model. *Atmos. Environ.,* **23,** 127–138.

McCumber, M. C., and R. A. Pielke, 1991: Simulations of the effects of surface fluxes of heat and moisture in a mesoscale numerical model. Part I: Soil layer. *J. Geophys. Res.,* **86,** 9929–9938.

O'Brien, J. J., 1970: A note on the vertical structure of the eddy exchange coefficient in the planetary boundary layer. *J. Atmos. Sci.,* **27,** 1213–1215.

Pérez-Muñuzuri, V., 1998: Forecasting of chaotic cloud absorption time series for meteorological and plume dispersion modeling. *J. Appl. Meteor.,* in press.

——, M. J. Souto, J. J. Casares, and V. Pérez-Villar, 1996: Terrain-induced focusing of wind fields in the mesoscale. *Chaos, Solitons Fractals,* **7,** 1479–1494.

Pielke, R. A., 1984: *Mesoscale Meteorological Modeling.* Academic Press, 612 pp.

——, and Y. Mahrer, 1975: Technique to represent the heated-planetary boundary layer in mesoscale models with coarse vertical resolution. *J. Atmos. Sci.,* **32,** 2288–2308.

——, and C. L. Martin, 1981: The derivation of a terrain-following coordinate system for use in a hydrostatic model. *J. Atmos. Sci.,* **38,** 1707–1713.

Prata, A. J., 1996: A new long-wave formula for estimating downward clear-sky radiation at the surface. *Quart. J. Roy. Meteor. Soc.,* **122,** 1127–1151.

Smeda, M. S., 1979: Incorporation of planetary boundary-layer processes into numerical forecasting models. *Bound.-Layer Meteor.,* **16,** 115–129.

Souto, J. A., V. Pérez-Muñuzuri, F. L. Ludwig, and J. J. Casares, 1994: Meteorological and atmospheric diffusion modeling for air pollution forecasting. *Computer Techniques in Environmental Studies,* V. P. Zannetti, Ed., Computational Mechanics, 281–288.

——, ——, M. DeCastro, J. J. Casares, and J. Abadía, 1996: Application of short and 24 hours air pollution forecasting around a power plant. *Air Pollution IV: Monitoring, Simulation and Control,* B. Caussade, H. Power, and C. A. Brebbia, Eds., Computational Mechanics, 21–30.

Stull, R. B., 1991: *An Introduction to Boundary Layer Meteorology.* Kluwer Academic, 666 pp.

Zhang, X., and A. F. Ghoniem, 1994: A computational model for the rise and dispersion of wind-blown, buoyancy-driven plumes—II: Linearly stratified atmosphere. *Atmos. Environ.,* **28,** 3005–3018.